Supplementary Information (SI) for Chemical Science.
This journal is © The Royal Society of Chemistry 2024

Electron Diffraction and Solid-state NMR Reveals Structure and Exciton Coupling in a Eumelanin Precursor

Kavya Vinod[a‡], Renny Mathew[b‡], Christian Jandl[c], Brijith Thomas[b]*, Mahesh Hariharan[a]*

[a]School of Chemistry, Indian Institute of Science Education and Research Thiruvananthapuram (IISER TVM), Maruthamala P.O., Vithura, Thiruvananthapuram, Kerala, 695551 (India)
[b]Science Division, New York University Abu Dhabi, P.O. Box 129188, Abu Dhabi, United Arab Emirates
[c]ELDICO Scientific AG, Switzerland Innovation Park Basel Area, Hegenheimermattweg 167A, 4123 Allschwil, Switzerland
E-mail: mahesh@iisertvm.ac.in

Table of Contents

Section 1. Materials and Methods:

All chemicals used for the synthesis were obtained from commercial suppliers and used as received without further purification. All reactions were carried out in oven-dried glassware before use and wherever necessary, were performed under dry nitrogen using standard gastight syringes, cannula, and septa. Solvents used for the spectroscopic measurements were dried and distilled by standard laboratory purification techniques. Yields refer to chromatographically and spectroscopically homogenous substances. IR spectra were recorded on a Shimadzu IRPrestige-21 FT-IR spectrometer as neat KBr pellets for all the derivatives. High resolution mass spectra (HRMS) were recorded on Thermo Scientific Q Exactive mass spectrometer using electrospray ionization (ESI, positive mode) technique. Photophysical measurements of the derivatives were carried out in a cuvette of 1 cm path length and concentration dependent measurements were performed in a cuvette of 1 mm path length. Absorption and emission spectra were recorded on UV-Vis-NIR Perkin Elmer Lambda 950 and Horiba Jobin Yvon Nanolog spectrometers respectively. The UV-Vis absorption spectra in the solution state were measured using the transmission mode and the Kubelka-Munk transformed reflectance spectra in the crystalline state were measured in the diffuse reflectance mode. The diffuse reflectance spectra allow no separation of the reflection, refraction and diffraction occurring from the crystalline samples.

Synthesis of DHICA

A solution of 1g (5 mmol, 1 eq.) L-DOPA in water (500 ml) and a solution of $K_3[Fe(CN)_6]$ (6.6 g, 20 mmol, 4 eq.) and $NaHCO_3$ (2.5 g, 30 mmol, 6 eq.) in water (60 ml) were separately degassed by purging with an argon flux for 10 min. The solution of $K_3[Fe(CN)_6]$ and $NaHCO_3$ was poured slowly to the solution of L-DOPA while vigorous stirring at room temperature. L-DOPA upon chemical oxidation using potassium ferricyanide turns into a wine-red solution of dopachrome. Within two minutes of stirring, 1 M solution of NaOH (70 mL) is added. The reaction mixture is allowed to stir for another 15 minutes. The reaction is maintained in a weakly basic medium that facilitates an oxidative nucleophilic reaction followed by the cyclisation of L-DOPA. Solid $Na_2S_2O_5$ (5.0 g, 26 mmol, 5.2 eq.) was then added to the dark brown solution, which was extracted with ethyl acetate (300 mL x 3). The ethyl acetate extracts were combined, washed once with saturated NaCl solution (100 mL), and dried over anhydrous Na_2SO_4 (50 g). Evaporation of ethyl acetate gave a brown oil to which a solution of hexane (20 mL) was added to give off-white powder of DHICA (Yield=76%). ^{13}C-labelled DHICA was synthesised using 0.2 g (1 mmol) of commercially bought ^{13}C-labelled L-DOPA with similar procedure as above, following the respective equivalencies (Yield=71%).

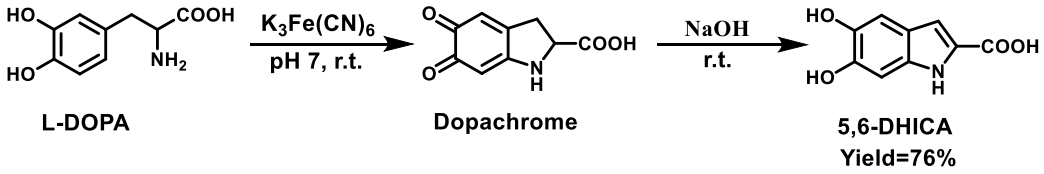

Scheme S1. Reaction scheme for the synthesis of DHICA from L-DOPA.

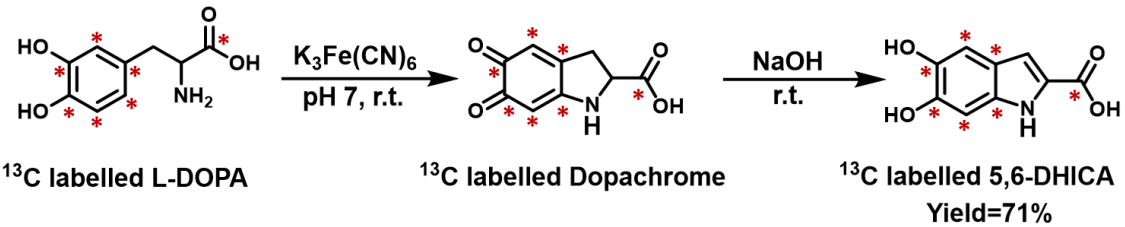

Scheme S2. Reaction scheme for the synthesis of ^{13}C-labelled DHICA from ^{13}C-labelled L-DOPA.

Synthesis of DHICA-melanin

Off-white powder of DHICA (500 mg) was dissolved in 200 mL of milliQ water. The solution was allowed to stir at ambient conditions for 7 days until the reaction mixture turned black. The black solution was centrifuged at 8000 rpm and the brown supernatant was decanted off. The precipitate was collected and washed multiple times with milliQ water.

The process was repeated until the supernatant was clear. Then the precipitate was further washed with acetone multiple times. The black solid was collected and air-dried to give 100-150 mg of DHICA-melanin.

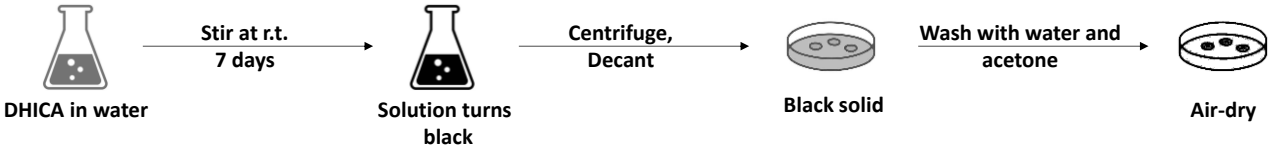

Scheme S3. Reaction scheme for the synthesis of unlabelled and ^{13}C labelled DHICA-melanin.

Solution state NMR

^{1}H and ^{13}C NMR in solution were measured on a 500 MHz Bruker Advance DPX spectrometer using 1,1,1,1-tetramethyl silane (TMS) as the internal standard. Data was processed using Mestrenova software.

3D electron diffraction

Samples were deposited on standard TEM grids (amorphous carbon on Cu) as dry powder after gentle grinding between microscope slides and measured in continuous rotation mode on an ELDICO *ED-1* electron diffractometer at room temperature using the software ELDIX. The device is equipped with a LaB_6 electron source operating at an acceleration voltage of 160 kV (λ = 0.02851 Å) and a hybrid-pixel detector (Dectris QUADRO). The grid was screened for suitable crystals in STEM (scanning transmission electron microscopy) mode and diffraction data were recorded in continuous rotation mode with a pseudo-parallel beam of ca. 750 nm diameter. Parts of measurements affected by beam damage or shadowing by the grid were omitted. Measurement details for all datasets used are given in Table S1.

Data were processed using the APEX4 software package.[2] Frames were integrated separately for each crystal, then merged, scaled, and corrected for Lorentz effects, scan speed, background, and absorption using SAINT and SADABS.[3,4] Space group assignment was based on systematic absences, E statistics, and successful refinement of the structure. The structure was solved using ShelXT and refined with ShelXL in conjunction with ShelXle.[5,6] Least squares refinements were carried out within the kinematic approximation by minimizing $\Sigma w(F_{obs}^2-F_{calc}^2)^2$ with the ShelXL weighting scheme and using neutral electron scattering factors.[5] Non-H atoms were refined with anisotropic displacement parameters and no restraints or constraints on non-H atoms were used in the refinement. H atoms were placed in calculated positions based on typical distances for neutron diffraction and refined as rigid rotating groups with $U_{iso}(H) = 1.5 \cdot U_{eq}(O)$ for hydroxy groups and with a standard riding model and $U_{iso}(H) = 1.2 \cdot U_{eq}(C/N)$ for other groups. Carboxylic acid protons were refined with the O-H bond lengths restrained to meet the expected neutron diffraction value and $U_{iso}(H) = 1.5 \cdot U_{eq}(O)$. Deposition Number 2347665 contains the supplementary crystallographic data for this paper. These data are provided free of charge by the joint Cambridge Crystallographic Data Centre and Fachinformationszentrum Karlsruhe Access Structures service and can be accessed at www.ccdc.cam.ac.uk/structures.

Solid-state NMR

All solid-state NMR spectra were measured with a Bruker Avance HD 600 WB NMR spectrometer operating at 14.1 T, corresponding to $\nu_0(^1H)$ = 600.5 MHz.

Experiments at 24 kHz: The fine powder of the samples was packed in a 3.2 mm outer diameter (o. d.) ZrO_2 rotor. For all experiments, the MAS speed was 24 kHz. The ^{1}H-^{13}C ramp-cross-polarization (rampCP) experiments were performed with a ^{13}C nutation frequency of 60 kHz, and the ^{1}H nutation frequency optimized at the +1 Hartman-Hahn condition ~84 kHz. The repetition delay was 2-3 s. $^{1}H\{^{13}C\}$ CP-HETCOR experiments were performed with a contact time of 50 µs and 1.0 ms, and 32-128 t_1 increments consisting of 256-512 scans were collected in each experiment. SPINAL64 decoupling (^{1}H B_1 field of ~83 kHz) was applied during acquisition. DUMBO homonuclear decoupling schemes were employed during the t_1 evolution at ~100 kHz. The ^{1}H scaling factor for DUMBO HETCOR was corrected using alanine as the standard, and ^{13}C shift scale were calibrated with adamantane as an external standard. All experiments were

performed at -30 degree Celsius. Several factors including slight exposure to air, humidity and/or light have been observed to cause the autoxidative polymerization of DHICA, wherein lowered temperatures decrease the kinetics of this solid-state polymerization.

Experiments at 60 kHz: Single-pulse ^{1}H spectra were recorded using 90° rf pulses operating at the ^{1}H nutation frequency $\nu_H \approx 185$ kHz, 16 accumulated NMR-signal transients, and relaxation delays (τ_{relax}) of 2.0 s. The ^{13}C spectra were recorded by the $^{1}H \rightarrow {}^{13}C$ CP at the double quantum Hartmann−Hahn condition, $\nu_H + \nu_C = \nu_r$, which involved ramped CP of $\nu_H = 20 \pm 5$ kHz for ^{1}H ($\nu_C = 40$ kHz), a 1.5 μs 90° ^{1}H pulse, and spinal-64 ^{1}H decoupling at $\nu_H = 150$ kHz. The $^{13}C\{^{1}H\}$ 2D HETCOR NMR spectra were recorded with $\tau_{CP} = 1.0$ ms $\tau_{relax} = 6.0$ s, and dwell times of $\Delta t_2 = 20.0$ μs and $\Delta t_1 = 5\tau r = 83.34$ us, where $\tau_r = \nu r^{-1}$ is the rotor period. $32(t_1) \times 2048(t_2)$ time points were collected with 2048 accumulated transients per t_1 value. The 2D NMR data sets were zero-filled to 64 t_1 points, along with 4096 (t_2), and were apodized by a $\cos^2$ and an exponential function along the indirect and direct dimensions, respectively, with the latter giving a 50 Hz full width at half-maximum (fwhm) Lorentzian broadening.[7]

The DQ−SQ ^{1}H NMR correlation spectra were recorded with the 2D NMR protocol shown in Figure 1a of ref [6]. The 2Q coherence (2QC) excitation/reconversion was accomplished by the BaBa dipolar recoupling scheme that extends over two rotor period,[6] thereby giving the 2Q excitation (τ_{exc}) and reconversion (τ_{rec}) intervals of $\tau_{exc} = \tau_{rec} = 2\tau_r = 33.33$ μs. The ^{1}H nutation frequency was $\nu_H \approx 185$ kHz for the 90° dipolar recoupling pulses of a duration of 1.35 μs. The 2D NMR acquisitions employed $\tau_{relax} = 2.0$ s, $48(t_1) \times 512(t_2)$ time points were acquired with dwell times of $\{\Delta t_1 = 2\tau_r; \Delta t_2 = 33.3$ μs$\}$ and 32 accumulated transients/t_1-value. The 2D data sets were zero-filled to 256 × 2048 points and apodized by an exponential 50 Hz fwhm Lorentzian broadening was applied both dimensions.

The CP-INADEQUATE were performed at a MAS rate of 60 kHz, and the ^{1}H and ^{13}C nutation frequencies were 160 and 130 kHz, respectively. The repetition delay was 6.0 s, and the evolution delays in refocused CP-INADEQUATE were 1 ms. A 256 t1 increments consisting of 64 transients were collected for both samples. SPINAL64 decoupling (^{1}H B_1 field of 150 kHz) was applied during both t_1 and t_2 periods.[8]

Experiments at 50 kHz: The ^{14}N chemical shifts were calibrated indirectly using established chemical shift standards and previously published relative NMR frequencies. Pulse sequence illustrations are provided in Figure S30. The DHMQC and RESPDOR[9] spectra were acquired at a 50 kHz MAS frequency. The magic angle for ^{1}H-^{14}N experiments was carefully set using KBr. The ^{1}H rf pulses were calibrated directly on each sample, and ^{1}H chemical shifts were referenced to neat tetramethylsilane ($\delta_{iso} = 0$ ppm), using adamantane ($\delta_{iso} = 1.85$ ppm) as a secondary standard. The ^{14}N chemical shifts were indirectly referenced using IUPAC frequency ratios, with all ^{14}N spectra referenced to the nitromethane scale. In all D-HMQC/RESPDOR experiments, the symmetry-based recoupling sequence $SR421$ was applied on the ^{1}H channel at the 2nd order rotary resonance recoupling condition. For $^{1}H\{^{14}N\}$ D-HMQC experiments, the optimal total dipolar recoupling times used for hist, and DHIC/DHIC-melanin were 160 μs, and 240 μs, respectively. For all $^{1}H\{^{14}N\}$ HMQC experiments, the ^{14}N excitation and reconversion pulse lengths had a duration of one rotor period, with an RF field of ~37 kHz. For the RESPDOR sequence (Figure S27) a saturation pulse (tsat) with a duration of 1.5 rotor cycles (30 μs with a 50 kHz MAS frequency) was applied on the ^{14}N channel, with an RF field of ~64 kHz. Experimental RESPDOR dipolar dephasing curves ($1 - S/S_0$) were obtained by measuring the ^{1}H NMR signal for each recoupling time without the ^{14}N dephasing pulse (S0) and with the 14N dephasing pulse (S). $^{1}H\{^{14}N\}$ RESPDOR curves were simulated using the SIMPSON (v4.1.1) program.

DFT calculations for structure prediction

The FORCITE module in the Materials studio was used for the initial relaxation of the structures with the Universal force field. Geometry optimizations were performed using the Smart algorithm with a convergence tolerance energy of 0.0001 kcal mol^{-1} and force of 0.005 kcal $Å^{-1}$ with a maximum number of iterations of 500. Plane-wave DFT calculations were done with the gauge-including projected augmented wave (GIPAW) approach as implemented in the CASTEP version 2017. Geometry optimization and NMR properties were calculated using the generalized gradient approximation (GGA) with the exchange-correlation PBESOL functional, with On-the-Fly ultra-Pseudopotential. Tkatchenko and Scheffler

method was employed for dispersion corrections in all optimizations. An energy cutoff of 900 eV with a Monkhorst−Pack grid with a k-point spacing of 0.05 $Å^{-1}$ was chosen to maximize the calculation efficiency and accuracy.

PXRD

Powder X-ray diffraction pattern was collected using Rigaku Smartlab X-ray diffractometer with Cu Kα radiation.

Transmission Electron Microscopy (TEM)

TEM measurements were carried out on FEI Tecnai 30 G2 high resolution transmission electron microscope and JEOL 2010 with an accelerating voltage of 100 kV. The samples were prepared by drop casting the DHICA solutions in milliQ water (100 μM and 1 mM), on a 400-mesh carbon-coated copper grid (Ted Pella, Inc.) at ambient conditions and allowing the excess solvent to evaporate in dust free conditions. TEM images were obtained without staining.

Scanning Electron Microscopy (SEM)

Scanning electron microscopy (SEM): SEM measurements were carried out on FEI Nova NanoSEM 450 (FEG type), drop casting DHICA-melanin on the flat surface of 400 mesh carbon-coated copper grid (Ted Pella, Inc.) and allowing to evaporate the excess solvent under air in dust free conditions. The sample was further subjected to thin chromium sputtering using JEOL JFC-1100 fine coater to increase the signal/noise ratio. The probing side was inserted into JEOL JSM-5600 LV scanning electron microscope for obtaining the images.

Dynamic light scattering (DLS)

DLS experiments were performed to examine the tendency of DHICA to undergo aggregation. Dynamic light scattering (DLS) measurements of DHICA in milliQ water (100 μM and 1 mM) was carried out on a Malvern Zeta Sizer Nano Zs equipped with 655 nm laser. The experiments were carried out in a 3 mL square glass cuvette at 25 ºC at a back scattering angle of 173º. DLS analysis of 100 μM DHICA in milliQ water displayed monomodal particle size distribution (D_H = 628 nm), whereas DLS analysis of 1 mM DHICA in milliQ water displayed bimodal particle size distribution (D_H = 487 nm and 2300 nm), indicating the formation of aggregates in high concentrated solutions.

Hirshfeld Analysis

Important intermolecular interactions within the structure of DMICE, BDMICE and IDMICE were identified through Hirshfeld surface analysis using CrystalExplorer17. The Hirshfeld surface is defined as a set of points in 3D space where the ratio of promolecule and procrystal electron densities is equal to 0.5. The exploration of intermolecular contacts is provided by mapping normalized contact distances (d_{norm}), which is a function of a closest distance from the point to the nuclei interior (d_i) and exterior (d_e) to the surface as well as on the van der Waals radii (r_{vdw}). 2D fingerprint plots derived from the Hirshfeld surface analyses, by plotting the fraction of points on the surface as the function of di and de, provides a visual summary of intermolecular contacts within the crystal.

Quantum Theory of Atoms in Molecules (QTAIM)

The wave function generation for the molecules was carried out at wb97xd/def2-svp using Gaussian 16 and the subsequent location of the critical points and the topology analysis were carried out using Multiwfn 3.7. Quantum theory of atoms in molecules (QTAIM) analyses helps to understand the description of interatomic interaction in the single crystal X-ray structure. A bond is defined along the bond line between two nuclei, called a bond path, along which electron density is concentrated. The (3, -1) bond critical point (BCP) is a point along the bond path at the interatomic surface, where the shared electron density reaches a minimum. (3, +1) ring critical point (RCP) and (3, +3) cage critical point (CCP) represents critical points in the ring and cage respectively where the electron density is minimum.

Symmetry Adapted Perturbation Theory (SAPT)

SAPT(0) analysis was employed to determine the non-covalent interaction energies of different non-covalent dimers of DMICE, BDMICE and IDMICE. The SAPT module of the psi4 code was employed, with def2-svp basis set. SAPT(0) calculations provide the contributing components of interaction energy. The results obtained from SAPT(0) analysis is a second order perturbation expansion constituting first order electrostatic and exchange energy parts and second order dispersion, induction and their exchange counterparts as the perturbation terms.

$$E_{int}^{SAPT(0)} = E_{elc}^{(1)} + E_{ex}^{(1)} + E_{ind}^{(2)} + E_{ind-ex}^{(2)} + E_{dis}^{(2)} + E_{dis-ex}^{(2)} \qquad \text{(Equation S8)}$$

Calculations on Exciton Interactions:

1) TheoDORE Analysis

The excitations of the different dimers obtained from the crystal structure were analyzed using TheoDORE. We study dimer systems, where each of the monomers is considered as a fragment (Figure S3-S5). The parameters used to investigate the excited state characteristics are participation ratio (PR), mean position (POS) of initial orbital (hole) and final orbital (electron), and charge transfer character (CT). The magnitude of PR relates to the number of fragments participating in the excitation; hence, in our investigation, the PR ranges from 1 to 2. POS provides the mean position of hole and electron for a particular excitation. Charge transfer states and delocalized Frenkel states show POS = 1.5. If the Frenkel state is localized on monomer A, then POS = 1, and if localized on monomer B, POS = 2, for a dimer AB. Finally, CT is related to the total weight of configurations where initial and final orbitals are situated on different fragments. A CT value of 1 denotes the presence of a charge-separated state, and CT = 0 refers to Frenkel states.

2) Electronic coupling calculations

All the calculations are carried out in Gaussian 16 employing the ωB97XD functional and 6-311G+(d,p) basis set at DFT level of theory unless stated otherwise. In order to compute long range Coulombic coupling, electronic energy transfer (EET) module available in gaussian 16 program is utilized. Electronic energy transfer (EET) or resonance energy transfer (RET) refers to the process of energy transfer from a photoexcited donor molecule to a nearby ground-state acceptor molecule. In Gaussian 16, the EET analysis employs a quantum mechanical model based on a DFT description of the wavefunction, incorporating a time-dependent variational approach. This involves performing an excited-state calculation on each fragment and subsequently computing all the couplings among the resulting states. J_{Coul} is the Coulombic coupling between electronic transitions where,

$$J_{Coul} = \iint dr_1 dr_2 \frac{\rho_D^{tr*}(r_1)\rho_A^{tr}(r_2)}{|r_1 - r_2|} \qquad \text{(Equation S1)}$$

Where, $\rho_D^{tr}(r_1)$ and $\rho_A^{tr}(r_2)$ are the transition densities (the diagonal element of the density matrix) respectively of donor and acceptor. TD-DFT calculation was performed on each of the dimers after defining each monomer as a fragment for the S_0 to S_1 transition and Coulombic coupling between the states was procured.

Electron and hole transfer coupling values were calculated by employing the CATNIP Tool version 1.9. CATNIP uses post-processed Gaussian 16 output files for the respective analyses. The short-range exciton coupling stemming from the degree of overlap of wave functions on proximal molecules has a crucial role in defining the excitonic interaction and is determined as,

$$J_{CT} = \frac{-2t_e t_h}{E_{CT} - E_{S_1}} \qquad \text{(Equation S2)}$$

where t_e and t_h are the electron and hole-transfer coupling which depend on the LUMO–LUMO and HOMO–HOMO orbital overlap of the monomers, respectively, E_{CT} is the energy of the charge-transfer state, and E_{S1} is the energy of first Frenkel exciton state calculated from TD-DFT. The total coupling between neighbouring molecules can be represented as,

$$J_{Total} = J_{Coul} + J_{CT} \qquad \text{(Equation S3)}$$

Section 2. Tables

Table S1: Previous attempts to elucidate the structure of eumelanin and its precursors.

Contributed by	**Journal**	**Methods employed to identify the aggregate structure**
Meredith and coworkers	Soft Matter, 2009, 5, 3754-3760	Low voltage–high resolution transmission electron microscopy
Bielawski, Paul, Freeman and coworkers	Langmuir, 2012, 28, 6428–6435	Solid state ^{15}N and ^{13}C-NMR, PXRD
Buehler and coworkers	Nat. Commun., 2014, 5, 3859	First-principles computational investigation
Warren and coworkers	ACS Nano, 2018, 12, 12050–12061	Transmission electron microscopy and pump-probe spectroscopy
Kohler and coworkers	Chem. Sci., 2020, 11, 1248-1259	Transmission electron microscopy and pump-probe spectroscopy
Hariharan and coworkers	Chem. Sci., 2022, 13, 2331-2338	Single-crystal X-ray diffraction
Hariharan, Thomas and coworkers	2024, current work	3D ED, solid-state NMR, DFT calculations

Table S2: 3D ED data collection details for the DHICA crystals used in refinement.

Crystal no.	**Approximate size [µm]**	**Angular range [°]**	**Rotation per frame [°]**	**Exposure time [s]**	**Total exposure [s]**	**Frames measured**	**Frames used**
1	0.4 x 0.3 x 0.2	−30 to +70	1	1	100	100	80
2	0.4 x 0.4 x 0.3	−60 to +50	1	1	110	110	110
3	0.5 x 0.3 x 0.2	−60 to +60	1	1	120	120	120

Table S3: The predicted ^{13}C NMR chemical shift and root mean square deviation for the case A.

Numbering scheme	**Solution state NMR** $\delta_{iso,sol}$ **(ppm)**	**Solid state NMR** $\delta_{iso,expt}$ **(ppm)**	**Difference** $\delta_{iso,sol}$ **-** $\delta_{iso,expt}$ **(ppm)**	**Chemical shielding** σ **(ppm)**	**Predicted chemical shift** $\delta_{iso,cal}$ **(ppm)**
C2	125.7	125.05	0.65	47.84	123.89
C3	107.9	115.39	-7.49	60.49	111.24
C4	104.6	107.70	-3.1	63.9	107.83
C5	146.2	139.68	6.52	32.11	139.62
C6	141.7	144.51	-2.81	25.96	145.77
C7	96.2	99.25	-3.05	76.38	95.35
C8	133.2	135.61	-2.41	37.34	134.39
C9	125.7	122.79	2.91	48.02	123.71
C10	163.9	167.28	-3.38	4.80	166.93
C2'	125.7	123.09	2.61	49.04	122.69
C3'	107.9	115.39	-7.49	57.33	114.40
C4'	104.6	107.70	-3.1	65.12	106.61
C5'	146.2	139.68	6.52	31.02	140.71
C6'	141.7	144.51	-2.81	27.24	144.49
C7'	96.2	97.59	-1.39	73.71	98.02
C8'	133.2	135.61	-2.41	37.51	134.22
C9'	125.7	122.79	2.91	49.47	122.26

C10'	163.9	165.32	-1.42	7.70	164.03
				RMSD	1.58

Table S4: The predicted ^{13}C NMR chemical shift and root mean square deviation for the case B.

Numbering scheme	**Solution state NMR $\delta_{iso,sol}$ (ppm)**	**Solid state NMR $\delta_{iso,expt}$ (ppm)**	**Chemical shielding σ (ppm)**	**Predicted chemical shift $\delta_{iso,cal}$ (ppm)**
C2	125.7	125.05	46.72	124.74
C3	107.9	115.39	55.75	115.71
C4	104.6	107.70	73.96	97.50
C5	146.2	139.68	27.69	143.77
C6	141.7	144.51	30.21	141.25
C7	96.2	99.25	66.43	105.03
C8	133.2	135.61	47.38	124.08
C9	125.7	122.79	37.81	133.65
C10	163.9	167.28	5.30	166.16
C2'	125.7	123.09	48.57	122.89
C3'	107.9	115.39	58.53	112.93
C4'	104.6	107.7	64.46	107.00
C5'	146.2	139.68	30.63	140.83
C6'	141.7	144.51	26.67	144.79
C7'	96.2	97.59	74.89	96.57
C8'	133.2	135.61	37.62	133.84
C9'	125.7	122.79	49.00	122.46
C10'	163.9	165.32	8.49	162.97
				4.92

Table S5: The predicted ^{13}C NMR chemical shift and root mean square deviation for the case C.

Numbering scheme	**Solution state NMR $\delta_{iso,sol}$ (ppm))**	**Solid state NMR $\delta_{iso,expt}$ (ppm)**	**Chemical shielding σ (ppm)**	**Predicted chemical shift $\delta_{iso,cal}$ (ppm)**
C2	125.7	125.05	47.12	124.52
C3	107.9	115.39	59.78	111.86
C4	104.6	107.70	64.65	106.99
C5	146.2	139.68	31.73	139.91
C6	141.7	144.51	26.58	145.06
C7	96.2	99.25	76.45	95.19
C8	133.2	135.61	37.74	133.90
C9	125.7	122.79	47.99	123.65
C10	163.9	167.28	4.47	167.17
C2'	125.7	123.09	49.51	122.13
C3'	107.9	115.39	56.23	115.41
C4'	104.6	107.70	73.7	97.94
C5'	146.2	139.68	26.18	145.46
C6'	141.7	144.51	30.44	141.20
C7'	96.2	97.59	64.68	106.96
C8'	133.2	135.61	48.48	123.16
C9'	125.7	122.79	38.72	132.92
C10'	163.9	165.32	8.75	162.89
			RMSD	5.40

Table S6: The predicted ^{13}C NMR chemical shift and root mean square deviation for the case D.

Numbering scheme	**Solution state NMR $\delta_{iso,sol}$ (ppm)**	**Solid state NMR $\delta_{iso,expt}$ (ppm)**	**Chemical shielding σ (ppm)**	**Predicted chemical shift $\delta_{iso,cal}$ (ppm)**
C2	125.7	125.05	46.3	125.32
C3	107.9	115.39	58.08	113.54
C4	104.6	107.70	75.08	96.54
C5	146.2	139.68	27.26	144.36
C6	141.7	144.51	30.84	140.78
C7	96.2	99.25	66.10	105.52
C8	133.2	135.61	47.55	124.07
C9	125.7	122.79	37.93	133.69
C10	163.9	167.28	4.87	166.75
C2'	125.7	123.09	49.68	121.94
C3'	107.9	115.39	56.93	114.69
C4'	104.6	107.7	73.43	98.19
C5'	146.2	139.68	25.70	145.92
C6'	141.7	144.51	29.60	142.02
C7'	96.2	97.59	66.41	105.21
C8'	133.2	135.61	48.77	122.85
C9'	125.7	122.79	38.66	132.96
C10'	163.9	165.32	9.74	161.88
			RMSD	7.18

Table S7: The predicted ^{1}H NMR chemical shift and root mean square deviation for the case A.

Numbering scheme	**Solution state NMR $\delta_{iso,sol}$ (ppm)**	**Solid state NMR $\delta_{iso,expt}$ (ppm)**	**Chemical shielding σ (ppm)**	**Predicted chemical shift $\delta_{iso,cal}$ (ppm)**
1NH	10.36	8.9	21.09	8.84
3	7.05	7.1	23.05	6.88
4	7.00	7.4	23.11	6.82
5 OH	7.78	9.2	20.68	9.25
6 OH	7.97	7.3	22.91	7.02
7	6.98	7.3	23.05	6.88
COOH	10.71	14.5*	14.94	14.99
1'NH	10.36	8.7	21.23	8.70
3'	7.05	6.5	23.77	6.16
4'	7.00	6.8	22.81	7.12
5' OH	7.78	9.8	19.90	10.03
6' OH	7.97	9.5	20.09	9.84
7'	6.98	6.8	23.21	6.72
COOH'	10.71	10.2	19.13	10.80
			RMSD	0.34

*The COOH peak assigned to 13.4 ppm based on the $^{1}H\{^{13}C\}$ HETCOR spectrum with a long contact time of 5 ms, results in an RMSD of 0.52 .

Table S8: The predicted ^{1}H NMR chemical shift and root mean square deviation for the case B.

Numbering scheme	Solution state NMR $\delta_{iso,sol}$ (ppm)	Solid state NMR $\delta_{iso,expt}$ (ppm)	Chemical shielding σ (ppm)	Predicted chemical shift $\delta_{iso,cal}$ (ppm)	Difference $\delta_{iso,expt} - \delta_{iso,cal}$ (ppm)
1	10.36	8.9	21.87	8.03	0.87
3	7.05	7.1	22.65	7.25	-0.15
4	7.00	7.4	23.06	6.84	0.56
5 OH	7.78	9.2	20.44	9.46	-0.26
6 OH	7.97	7.3	23.4	6.50	0.80
7	6.98	7.3	22.74	7.16	0.14
COOH	10.71	14.5*	14.15	15.75	-2.35
1'	10.36	8.7	21.88	8.02	0.68
3'	7.05	6.5	23.67	6.23	0.27
4'	7.00	6.8	22.74	7.16	-0.36
5' OH	7.78	9.8	19.72	10.18	-0.38
6' OH	7.97	9.5	19.96	9.94	-0.44
7'	6.98	6.8	23.24	6.66	0.14
COOH'	10.71	10.2	19.12	10.78	-0.58
				RMSD	0.58

*The COOH peak assigned to 13.4 ppm based on the $^{1}H\{^{13}C\}$ HETCOR spectrum with a long contact time of 5 ms, results in an RMSD of 0.78.

Table S9: The predicted ^{1}H NMR chemical shift and root mean square deviation for the case C.

Case C					
Numbering scheme	**Solution state NMR $\delta_{iso,sol}$ (ppm)**	**Solid state NMR $\delta_{iso,expt}$ (ppm)**	**Chemical shielding σ (ppm)**	**predicted chemical shift $\delta_{iso,cal}$ (ppm)**	**Difference $\delta_{iso,expt} - \delta_{iso,cal}$ (ppm)**
1	10.36	8.9	21.28	8.66	0.24
3	7.05	7.1	22.94	7.00	0.10
4	7.00	7.4	23.07	6.87	0.53
5 OH	7.78	9.2	20.78	9.16	0.04
6 OH	7.97	7.3	22.69	7.25	0.05
7	6.98	7.3	23.04	6.90	0.40
COOH	10.71	14.5*	15.16	14.78	-1.38
1'	10.36	8.7	22.76	7.18	1.52
3'	7.05	6.5	22.91	7.03	-0.53
4'	7.00	6.8	22.95	6.99	-0.19
5' OH	7.78	9.8	19.43	10.51	-0.71
6' OH	7.97	9.5	19.56	10.38	-0.88
7'	6.98	6.8	22.93	7.01	-0.21
COOH'	10.71	10.2	19.65	10.29	-0.09
				RMSD	0.57

*The COOH peak assigned to 13.4 ppm based on the $^{1}H\{^{13}C\}$ HETCOR spectrum with a long contact time of 5 ms, results in an RMSD of 0.67.

Table S10: The predicted ^{1}H NMR chemical shift and root mean square deviation for the case D.

Case D					
Numbering scheme	**Solution state NMR $\delta_{iso,sol}$ (ppm)**	**Solid state NMR $\delta_{iso,expt}$ (ppm)**	**Chemical shielding σ (ppm)**	**Predicted chemical shift $\delta_{iso,cal}$ (ppm)**	**Difference $\delta_{iso,expt} - \delta_{iso,cal}$ (ppm)**
1	10.36	8.9	21.82	8.17	0.73
3	7.05	7.1	22.86	7.13	-0.03
4	7.00	7.4	23.11	6.88	0.52
5 OH	7.78	9.2	20.64	9.35	-0.15
6 OH	7.97	7.3	23.33	6.66	0.64
7	6.98	7.3	22.77	7.22	0.08

COOH	10.71	14.5*	14.33	15.66	-2.26
1'	10.36	8.7	22.65	7.34	1.36
3'	7.05	6.5	23.28	6.71	-0.21
4'	7.00	6.8	23.04	6.95	-0.15
5'OH	7.78	9.8	19.51	10.48	-0.68
6'OH	7.97	9.5	19.6	10.39	-0.89
7'	6.98	6.8	23.08	6.91	-0.11
COOH'	10.71	10.2	19.89	10.10	0.10
				RMSD	0.64

*The COOH peak assigned to 13.4 ppm based on the $^{1}H\{^{13}C\}$ HETCOR spectrum with a long contact time of 5 ms, results in an RMSD of 0.82.

Table S11: Comparison of energy for cases A, B, C and D along with the RMSD of ^{1}H chemical shift.

Label	Final Energy (eV)	^{1}H RMSD (ppm)
Case A	-14234.94	0.34
Case B	-14234.68	0.58
Case C	-14234.75	0.57
Case D	-14234.61	0.64

Table S12: Interaction energies[a] of DHICA dimers evaluated using symmetry-adapted perturbation theory (SAPT(0)) aug-cc-pVDZ calculations.

Dimer	E_{int}^{SAPT}	Electrostatic Energy (E_{elc})	Dispersion Energy (E_{dis})	Induction Energy (E_{ind})	Exchange Energy (E_{ex})
D1	-12.09	-3.42	-18.91	-0.86	11.09
D2	-11.65	-5.64	-15.42	-0.99	10.41
D3	-13.22	-6.93	-18.88	-1.65	14.24
D4	-7.66	-15.29	-6.61	-6.65	20.89
D5	-7.36	-10.09	-5.26	-2.41	10.40
D6	-25.75	-36.46	-8.57	-17.83	37.11
All energy values are given in kcal/mol.					

Table S13: Fragment based excited state analysis for dimer D1 in the crystalline assembly of DHICA.

State	dE(eV)	f	POS	PR	CT
S1	3.874	0.000	1.500	2.000	0.214
S2	4.143	0.000	1.500	2.000	0.139
S3	4.269	0.470	1.500	2.000	0.055
S4	4.323	0.414	1.500	2.000	0.106
S5	4.512	0.023	1.500	2.000	0.864
S6	4.630	0.000	1.500	2.000	0.789
S7	4.883	0.020	1.500	2.000	0.959
S8	4.985	0.000	1.500	2.000	0.836
S9	5.254	0.094	1.500	2.000	0.216
S10	5.322	0.001	1.469	1.992	0.019

Table S14: Fragment based excited state analysis for dimer D2 in the crystalline assembly of DHICA.

State	dE(eV)	f	POS	PR	CT
S1	3.944	0.000	1.500	2.000	0.172
S2	4.253	0.095	1.500	2.000	0.084
S3	4.274	0.930	1.500	2.000	0.044
S4	4.301	0.046	1.500	2.000	0.029
S5	4.635	0.000	1.500	2.000	0.918
S6	4.755	0.000	1.500	2.000	0.809
S7	5.173	0.000	1.500	2.000	0.906
S8	5.222	0.018	1.500	2.000	0.799
S9	5.314	0.000	1.437	1.968	0.056
S10	5.317	0.004	1.564	1.968	0.118

Table S15: Fragment based excited state analysis for dimer D3 in the crystalline assembly of DHICA.

State	dE(eV)	f	POS	PR	CT
S1	4.235	0.000	1.499	2.000	0.033
S2	4.246	1.036	1.501	2.000	0.062
S3	4.398	0.000	1.494	2.000	0.074
S4	4.419	0.072	1.506	2.000	0.055
S5	4.955	0.000	1.500	1.998	0.881
S6	4.966	0.010	1.500	1.998	0.890
S7	5.082	0.000	1.144	1.327	0.007
S8	5.083	0.000	1.856	1.327	0.008
S9	5.213	0.000	1.500	2.000	0.615
S10	5.333	0.031	1.500	2.000	0.867

Table S16: Fragment based excited state analysis for dimer D4 in the crystalline assembly of DHICA.

State	dE(eV)	f	POS	PR	CT
S1	4.106	1.234	1.568	1.964	0.005
S2	4.211	0.007	1.431	1.963	0.003
S3	4.303	0.120	1.026	1.053	0.002
S4	4.400	0.066	1.976	1.049	0.003
S5	5.319	0.000	2.000	1.001	0.001
S6	5.461	0.130	1.972	1.058	0.042
S7	5.481	0.048	1.044	1.096	0.084
S8	5.508	0.001	1.069	1.153	0.120
S9	5.526	0.060	1.190	1.447	0.353
S10	5.540	0.023	1.244	1.524	0.429

Table S17: Fragment based excited state analysis for dimer D5 in the crystalline assembly of DHICA.

State	dE(eV)	f	POS	PR	CT
S1	4.258	1.290	1.500	1.500	0.003
S2	4.346	0.000	1.500	1.500	0.002
S3	4.485	0.001	1.566	1.566	0.002
S4	4.487	0.102	1.434	1.434	0.002

S5	5.070	0.000	2.000	1.001	0.000
S6	5.070	0.000	1.000	1.001	0.000
S7	5.520	0.001	1.545	1.984	0.009
S8	5.521	0.279	1.455	1.984	0.005
S9	5.611	0.000	1.498	2.000	0.136
S10	5.664	0.011	1.503	2.000	0.102

Table S18: Fragment based excited state analysis for dimer D6 in the crystalline assembly of DHICA.

State	**dE(eV)**	**f**	**POS**	**PR**	**CT**
S1	4.186	1.393	1.500	2.000	0.009
S2	4.348	0.000	1.500	2.000	0.005
S3	4.421	0.006	1.252	1.605	0.005
S4	4.421	0.088	1.748	1.604	0.004
S5	5.482	0.155	1.496	2.000	0.011
S6	5.499	0.000	1.504	2.000	0.004
S7	5.530	0.124	1.500	2.000	0.008
S8	5.556	0.000	1.500	2.000	0.029
S9	5.572	0.000	1.500	2.000	0.061
S10	5.599	0.007	1.500	2.000	0.062

Table S19: T_1 measurement of the samples

SI No.	**Compound**	**T_1**
1	DHI	100 s
2	DHICA	4 s
3	DHICA melanin	0.7 s

Table S20: Summary of the observed similarities and differences between monomer and polymer.

Technique	**DHICA**	**DHICA-melanin**
SEM	Globular	Layered/sheet arrangements
FT-IR	NH stretching band at 3435 cm^{-1} OH and COOH stretching bands at 3265 cm^{-1}	NH stretching band at 3435 cm^{-1} OH and COOH stretching bands at 3265 cm^{-1} sp^3 -CH stretching peak at 2980 cm^{-1}
UV-Visible absorption	Absorption spectrum is broad and ranges from 200-570 nm in crystalline state compared to monomeric solution	Broad absorption ranges from 200-1400 nm
Solubility	Soluble but difficult to crystalize	Insoluble
3D ED	Triclinic space group $P\bar{1}$ with a=7.49 Å, b=10.23 Å, c=10.81 Å, α=82.27°, β=87.80°, γ=70.10°	Broad diffraction pattern
Solid-state NMR	No aliphatic moiety	Observation of aliphatic peaks
	Only one nitrogen species with a broad NMR spectrum	Multiple nitrogen species
	-	Distribution of chemical shift in the case of C7
	N-H peaks are observed around 9 ppm	N-H peaks are observed around 11 ppm
	Observation of carbonyl group	Observation of carbonyl group
	Presence of carboxylic acid proton	Absence of carboxylic acid proton

Section 3. Figures

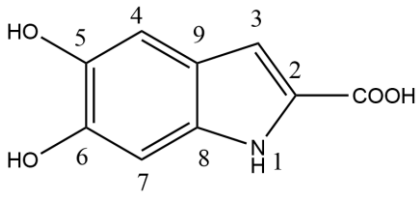

Figure S1: The chemical structure of 5,6-dihydroxyindole-2-carboxylic acid (DHICA) along with numbering scheme used in the manuscript.

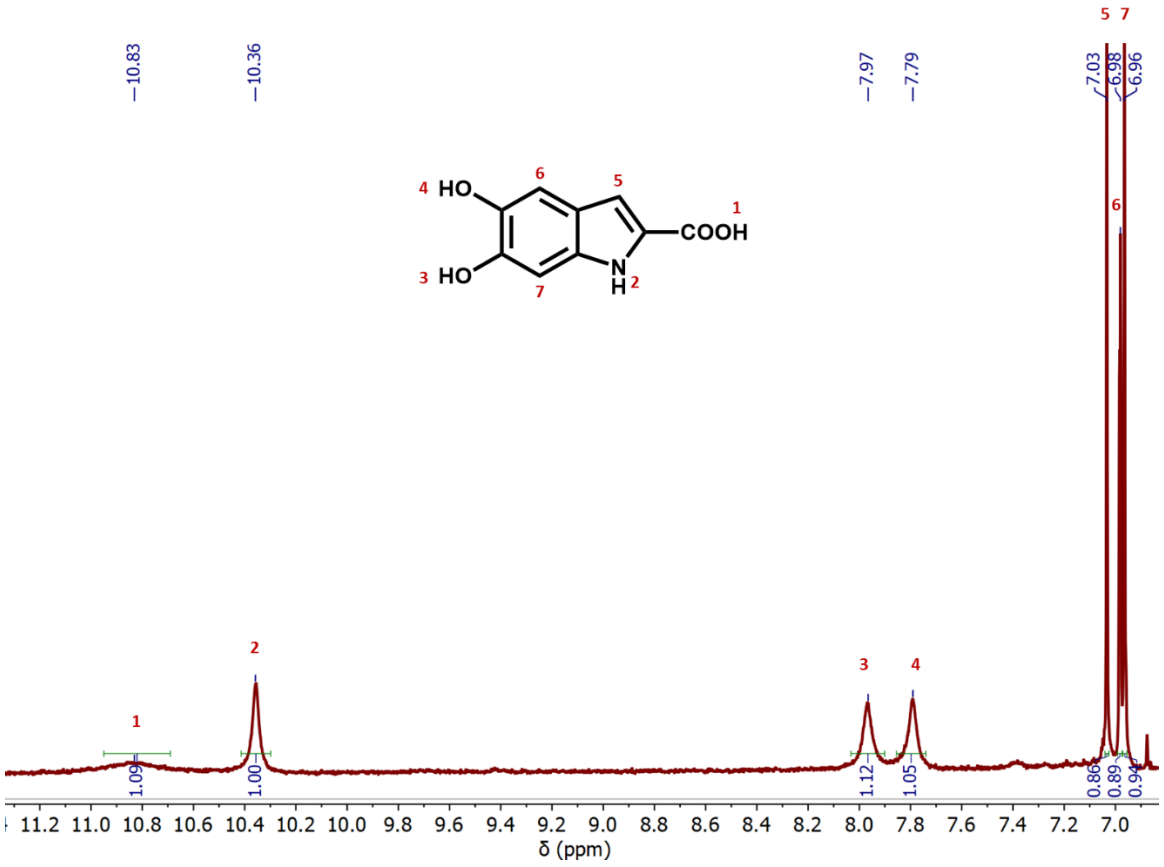

Figure S2: Solution-state ^{1}H-NMR spectra of DHICA.

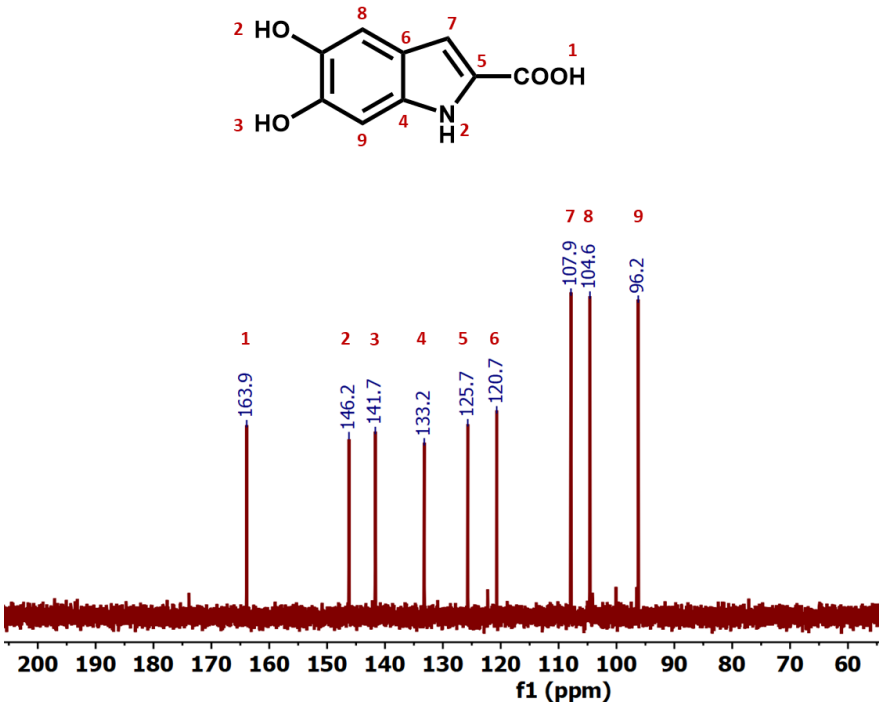

Figure S3: Solution-state ^{13}C-NMR of DHICA.

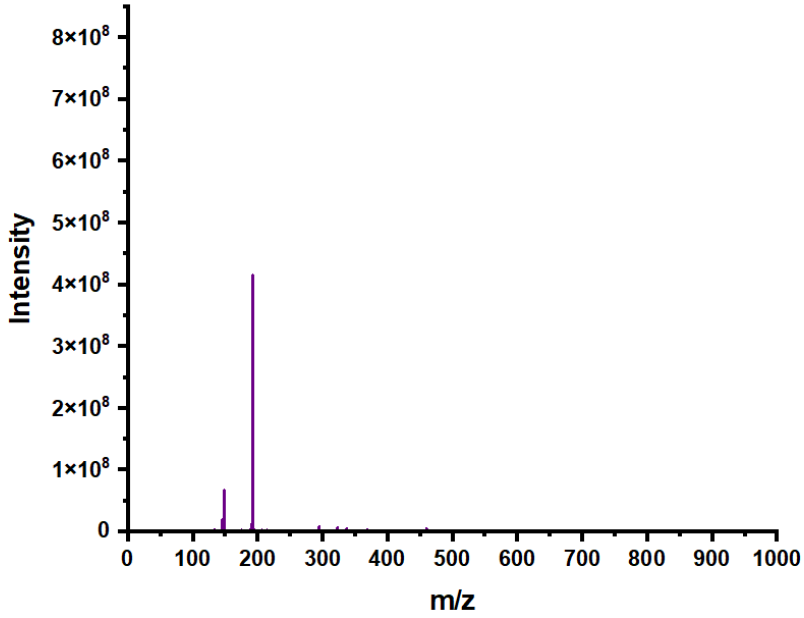

Figure S4: The HRMS spectrum of DHICA.

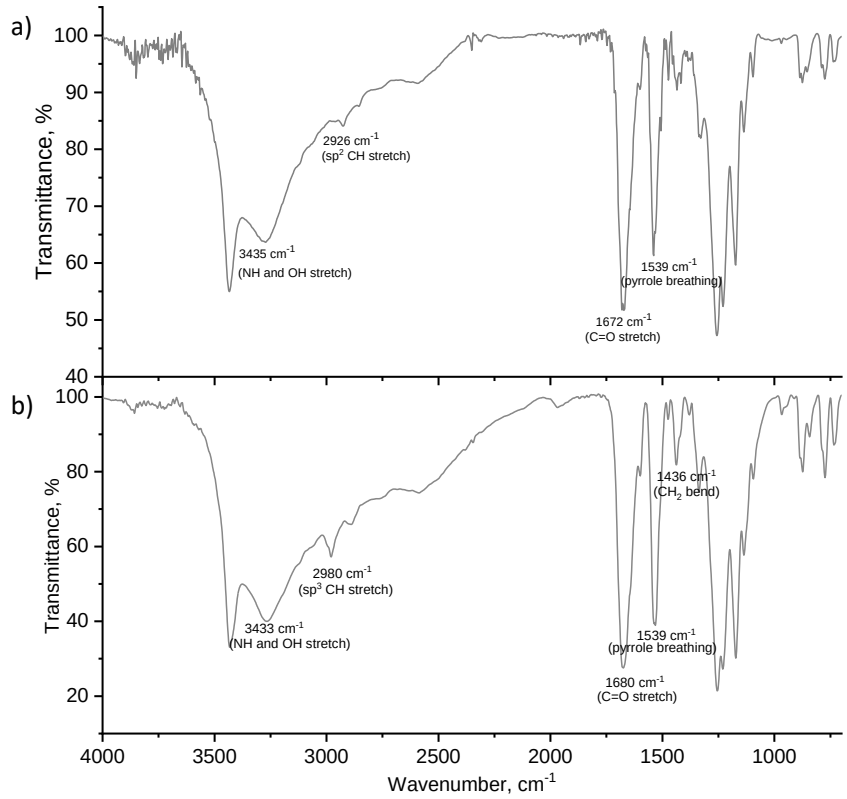

Figure S5: FT-IR spectra of a) DHICA and b) DHICA-melanin in KBr pellets.

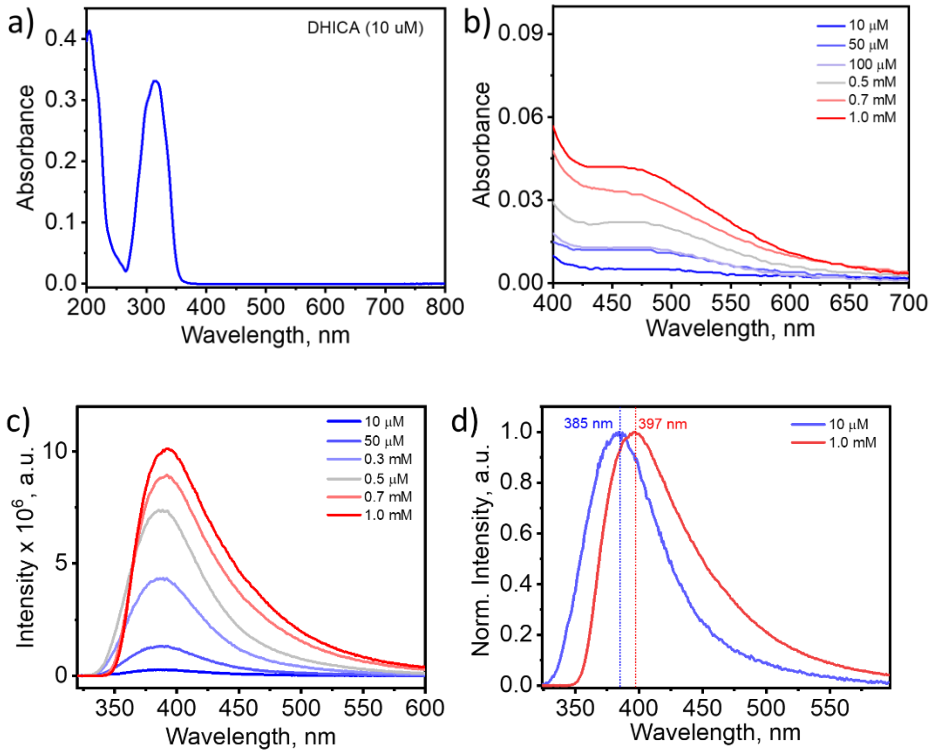

Figure S6: a) UV-Vis absorption spectrum of DHICA in milliQ water (10 µM); b) Concentration dependent absorption spectra of DHICA in water (10 µM-1 mM), showing the emergence of the aggregate band as concentration increases; c)

Concentration dependent fluorescence spectra of DHICA in water (10 µM-1 mM); d) Normalized fluorescence spectra of DHICA in water at 10 µM and 1 mM, showing the red-shift in the fluorescence maxima with increase in concentration.

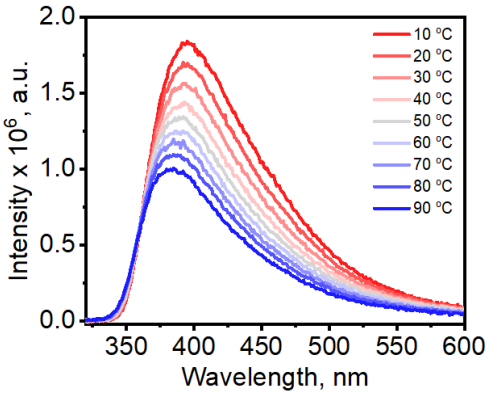

Figure S7: Temperature dependent fluorescence emission of DHICA in water at 1 mM concentration.

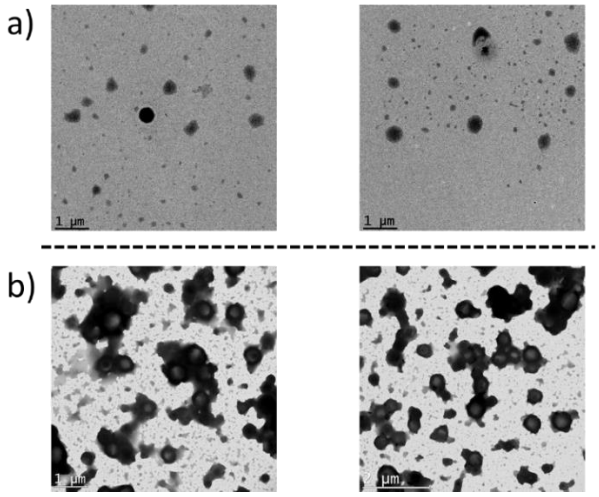

Figure S8. TEM images of a) 100 µM DHICA and b) 1 mM DHICA in water, showing the aggregate formation at higher concentrations.

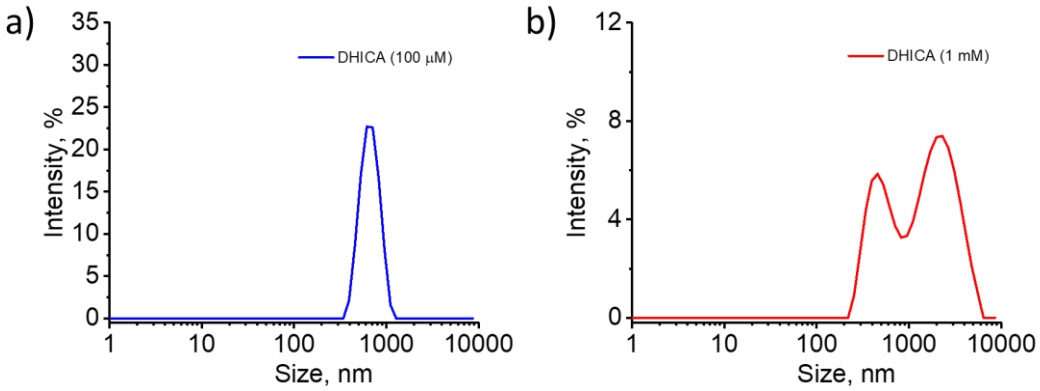

Figure S9. DLS size profiles of a) 100 µM DHICA and b) 1 mM DHICA in water, showing the aggregate formation with increase in particle size at higher concentrations.

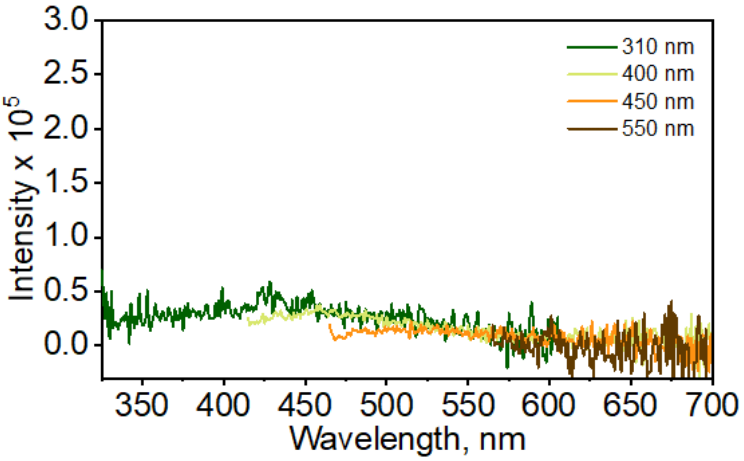

Figure S10. Fluorescence emission spectrum of DHICA-melanin in the solid state at different excitation wavelengths.

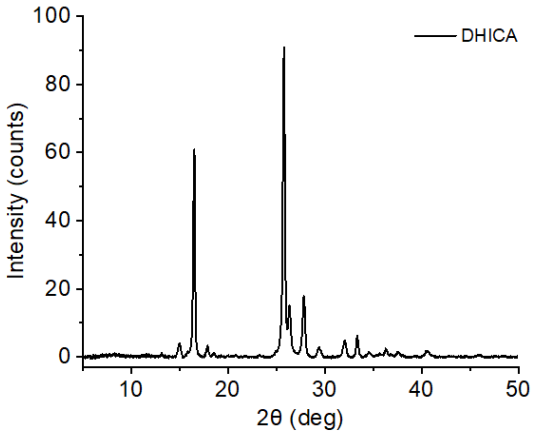

Figure S11: The powder X-ray diffraction pattern of DHICA collected at room temperature.

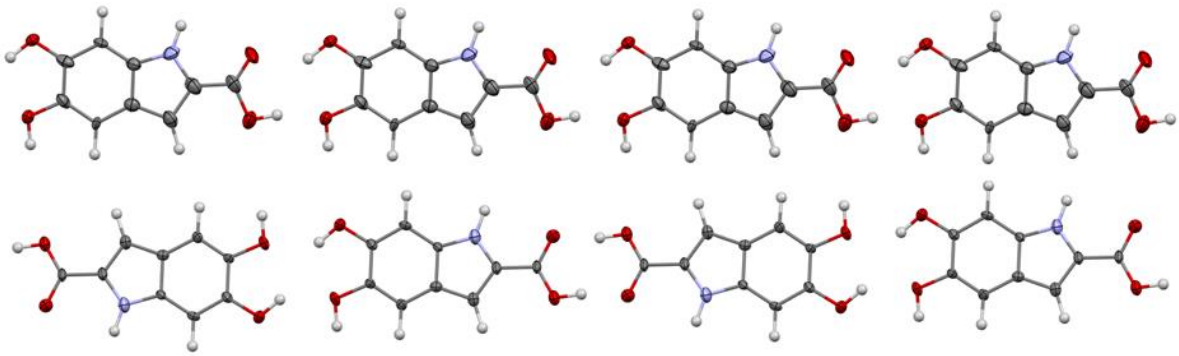

Figure S12: Two different chain motifs in the crystalline assembly of DHICA: head-to-tail (top), head-to-head (bottom). Motifs correspond to the two independent molecules and are uniform within each layer.

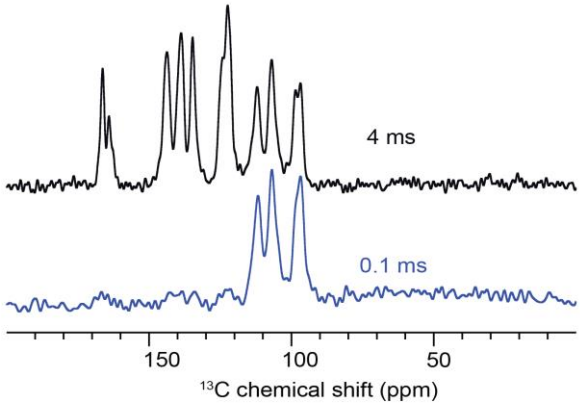

Figure S13: Comparative ^{13}C Cross-Polarization solid-state NMR spectra of unlabelled DHICA monomer at -30°C and a spinning rate of 24 kHz, recorded at contact times of 0.1 ms (bottom) and 1 ms (top). Two clearly distinguishable sets of peaks are observable for the carboxylic acid group, suggesting that molecules are present in two asymmetrical locations.

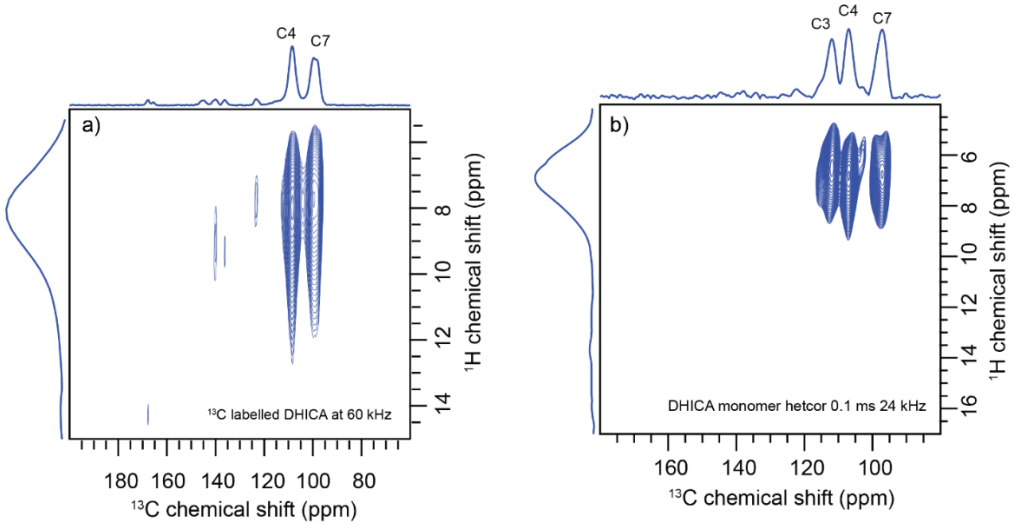

Figure S14: The two dimensional ^{1}H-^{13}C HETCOR spectra of a) ^{13}C labelled DHICA and b) unlabelled DHICA collected at a contact time of 0.1 ms.

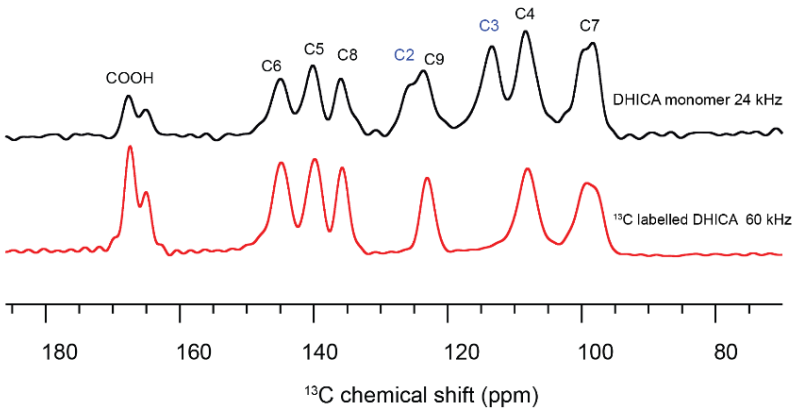

Figure S15: Comparative ^{13}C Cross-Polarization solid-state NMR spectra of unlabelled and ^{13}C labelled DHICA monomer at -30°C and a spinning rate of 24 kHz and 60 kHz respectively.

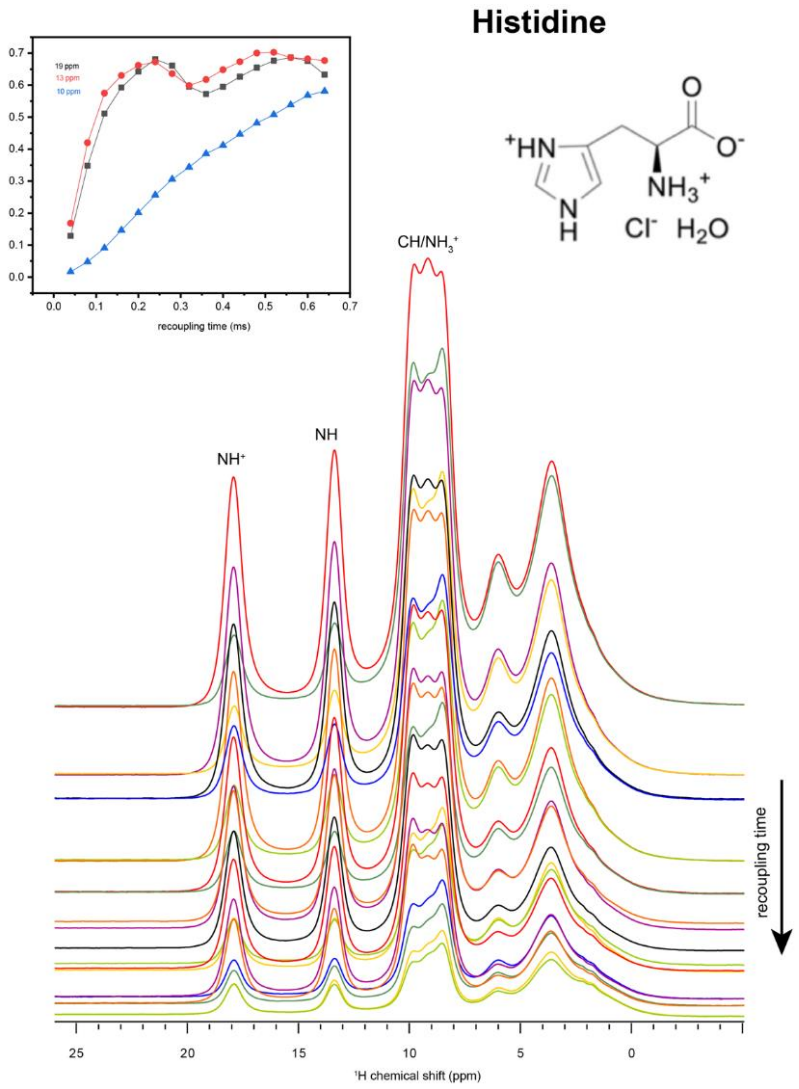

Figure S16: The $^{1}H\{^{14}N\}$ RESPDOR curve of histidine hydrate monochloride obtained at a spinning speed of 60 kHz.

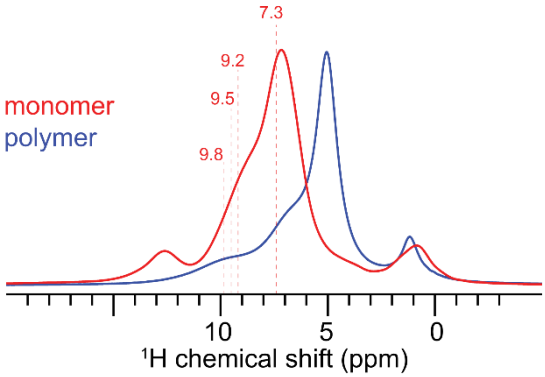

Figure S17: The solid-state ^{1}H NMR spectra of DHICA and DHICA-melanin. The marked positions (dotted vertical lines), correspond to chemical shift assignments of the hydroxyl protons of DHICA, based on DFT calculations. A shift towards higher field in the chemical shift is observed for the main aromatic peak. An aliphatic peak is also seen at around 1 ppm. DHICA is precipitated out using hexane and washed with hexane to give the off-white powder. The aliphatic peaks at 1.29 and 0.88 ppm are probably due to the trace amounts of hexane. The absence of these same proton signals in the ^{1}H-^{13}C HETCOR spectra may be attributed to the mobility of hexane.

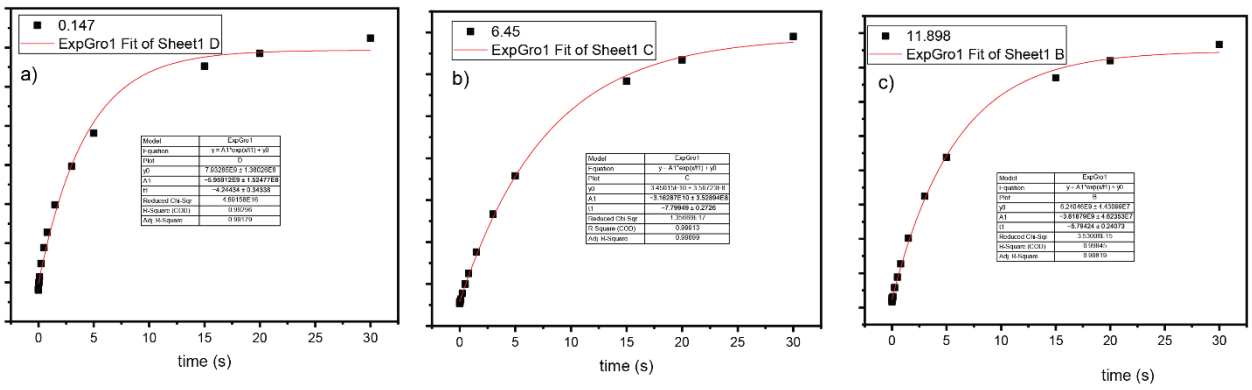

Figure S18: The ^{1}H magnetization build up curves obtained using saturation recovery experiment at 60 kHz spinning speed.

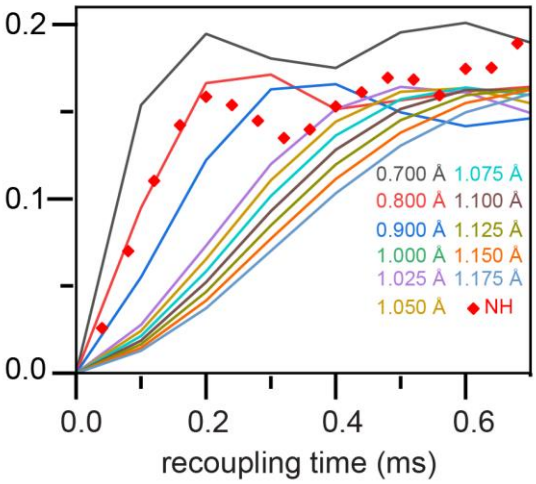

Figure S19: The $^{1}H\{^{14}N\}$ RESPDOR curve of DHICA along with the simulation using simpson. Relative low dephasing compared to histidine might be due to the overlap of proton peaks.

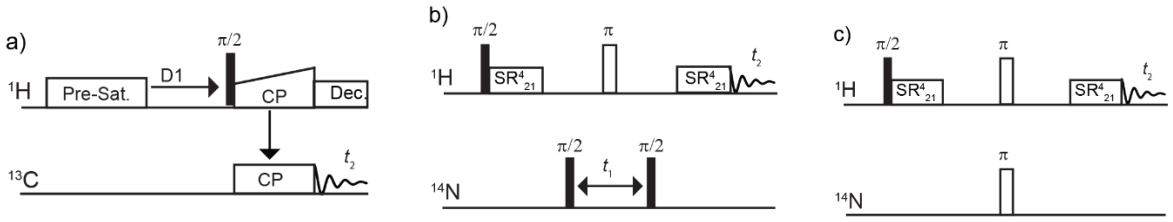

Figure S20: Pulse sequence used for the solid-state NMR measurements a) $^{1}H\{^{13}C\}$ CP HETCOR b) $^{1}H\{^{14}N\}$ DHMQC and c) $^{1}H\{^{14}N\}$ RESPDOR.

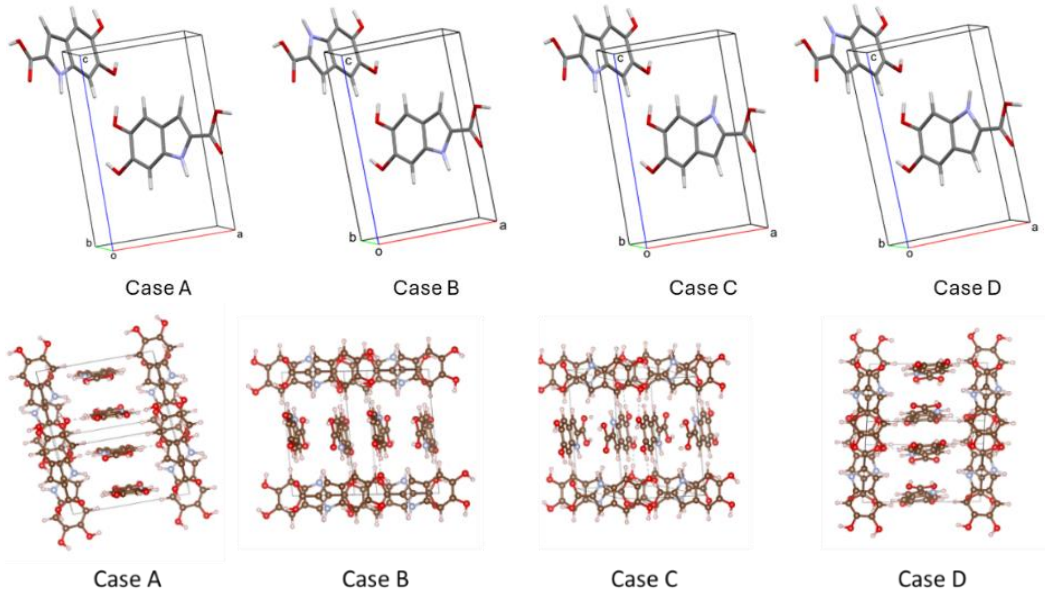

Figure S21: The four different cases used for the DFT calculation and NMR chemical shift prediction of DHICA (top: asymmetric unit, bottom: packing).

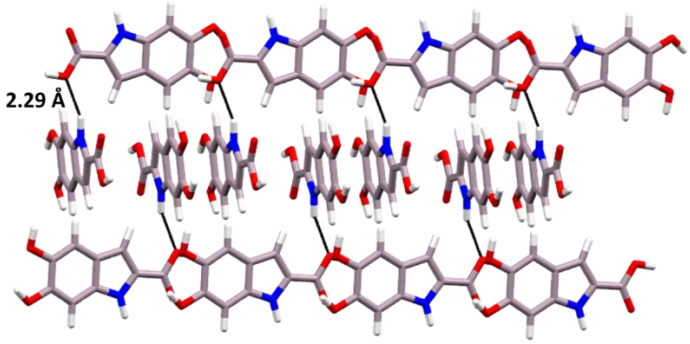

Figure S22. Interchain N-H•••O contacts for the DHICA units.

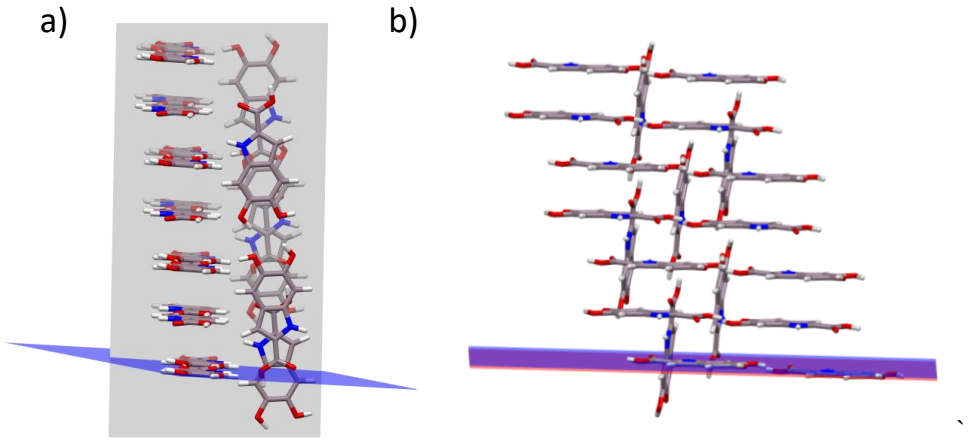

Figure S23. a) The near-orthogonal and b) co-linear stacks in the crystal assembly of DHICA.

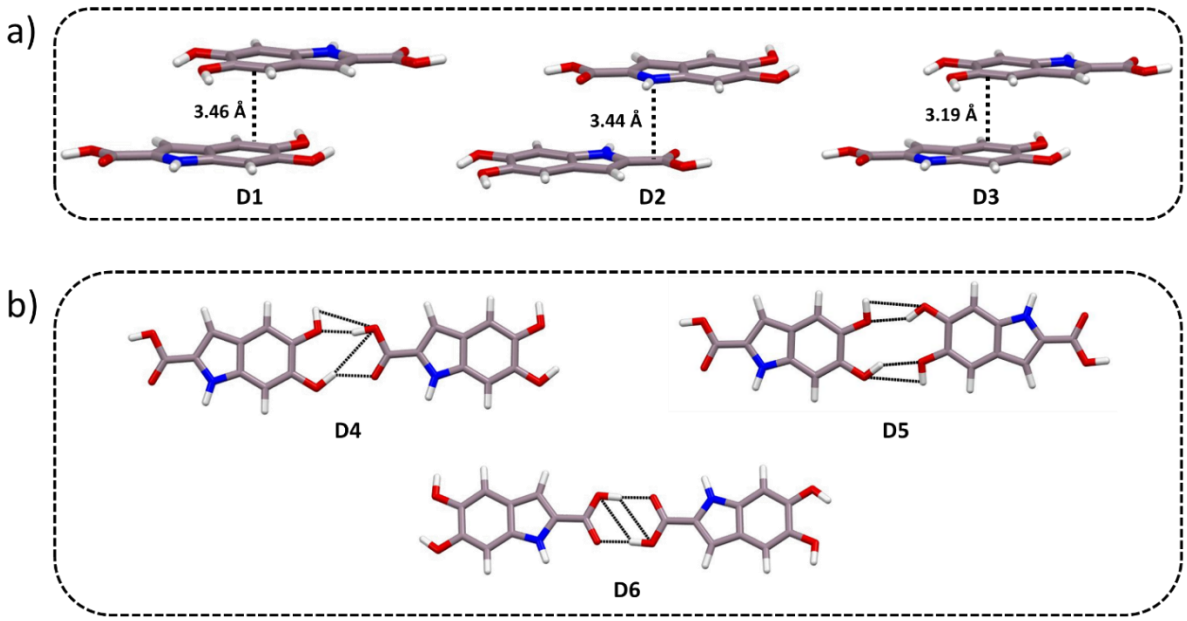

Figure S24: Different orientations of DHICA motifs in the crystal. a) π-π stacked dimers (D1–D3) and b) the hydrogen-bond directed dimers (D4-D6) observed in the crystal.

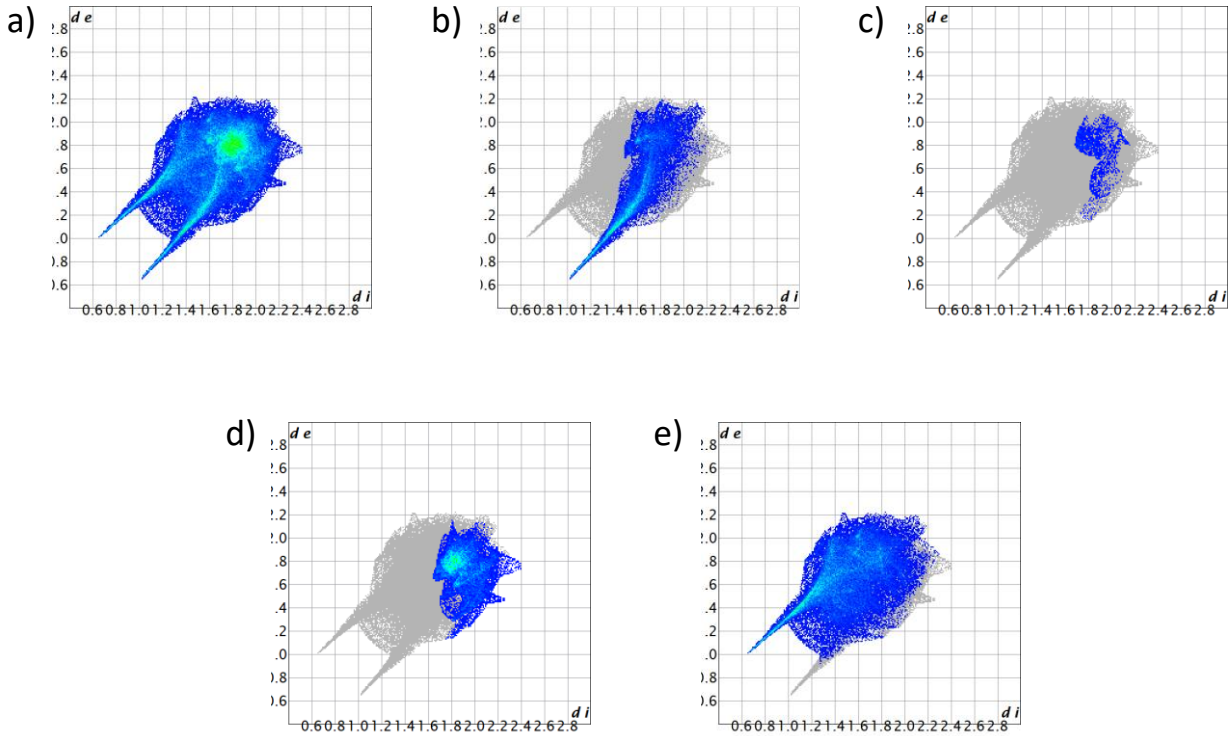

Figure S25. Hirshfeld surface plot for a) contacts from all elements, b) contacts from O, c) contacts from N, d) contacts from C and e) contacts from H.

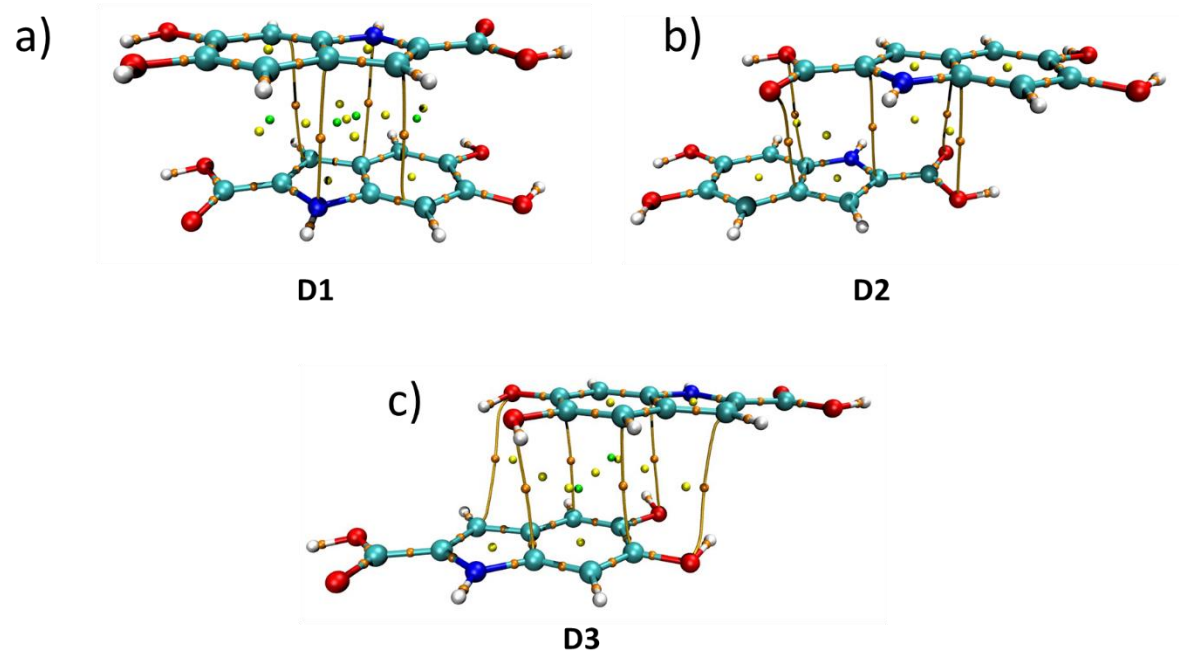

Figure S26: QTAIM electron density maps showing the synthon formation from π-π stacking in DHICA dimers a) D1, b) D2 and c) D3.

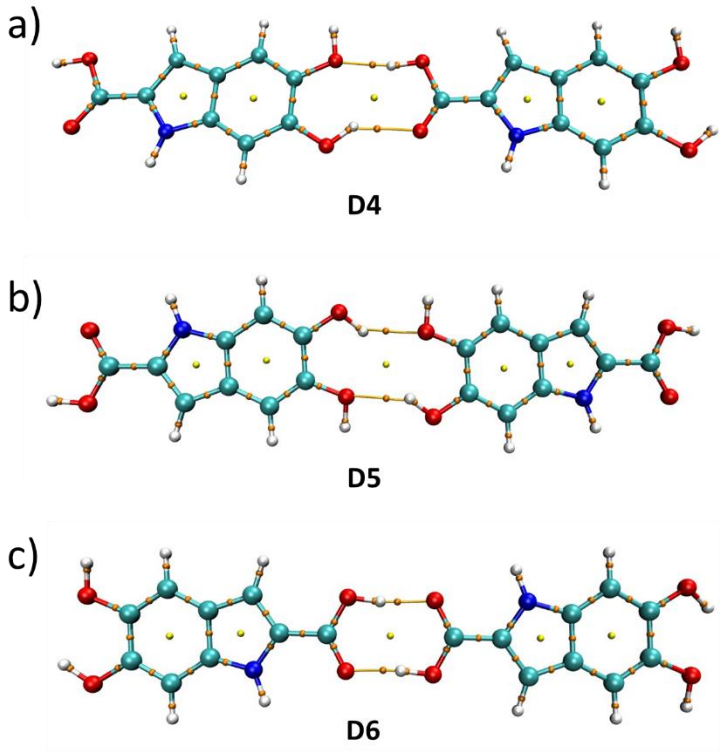

Figure S27: QTAIM electron density maps showing the synthon formation from hydrogen bonding interactions in DHICA dimers a) D4, b) D5 and c) D6.

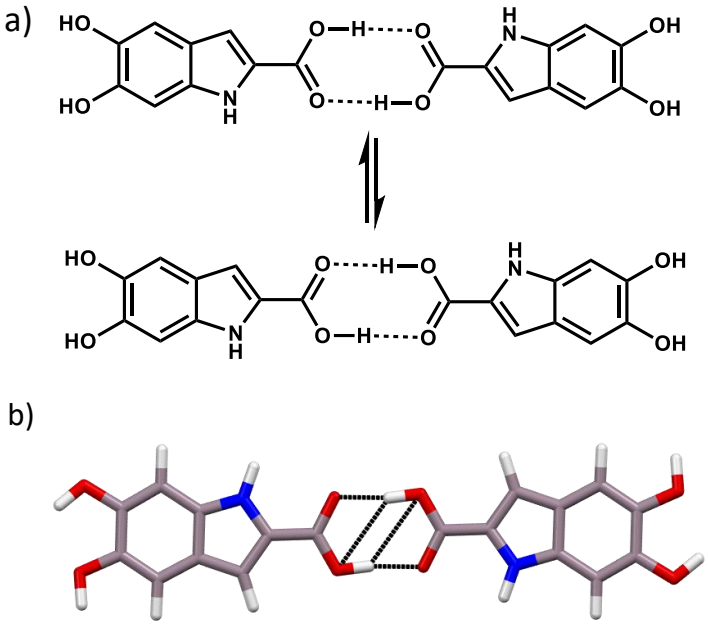

Figure S28: The D6 dimer in DHICA showing a) resonance assisted hydrogen bond (RAHB); b) bifurcated hydrogen bonding.

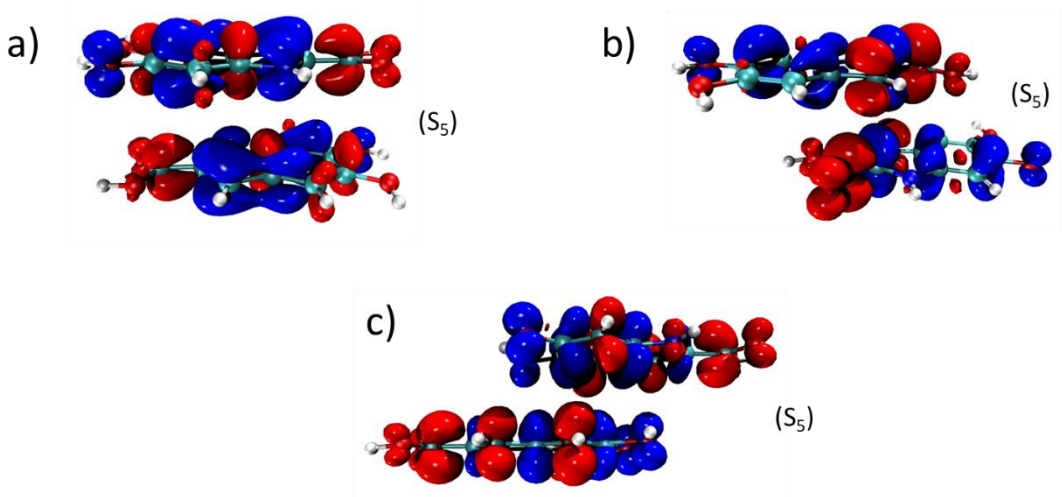

Figure S29: The charge-density difference plots (iso-value=0.0008 e-bohr^{-3}) for a) D1 dimer, b) D2 dimer and c) D3 dimer. The red represents the positive and blue represents negative values respectively.

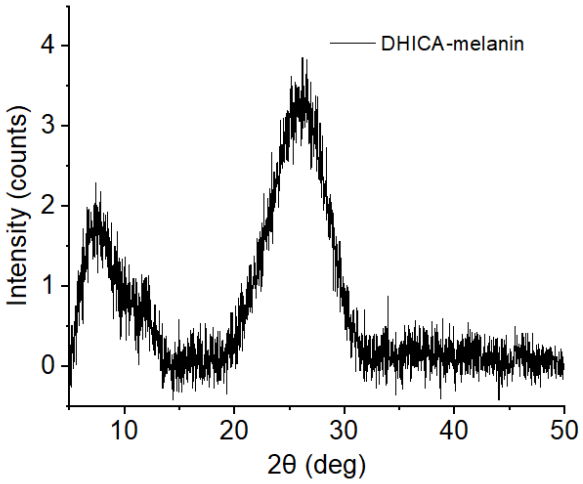

Figure S30: The powder X-ray diffraction pattern of DHICA-melanin collected at room temperature.

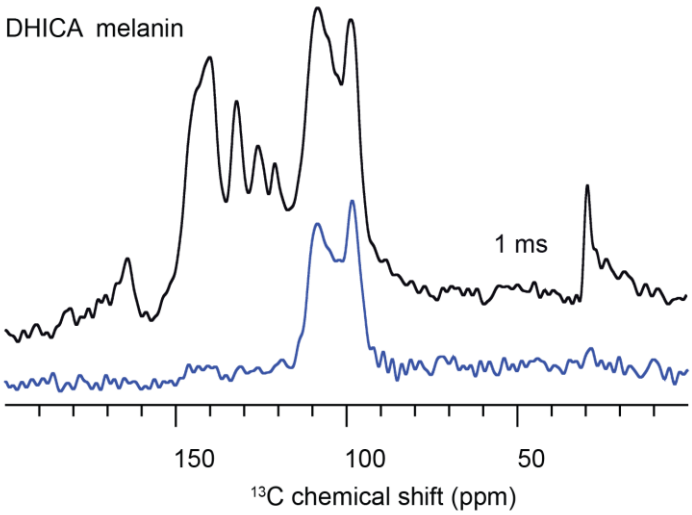

Figure S31: The ^{13}C Cross-Polarization solid-state NMR spectra of unlabelled DHICA-melanin at -30°C with a spinning rate of 24 kHz. Spectra were collected at two different contact times: 0.1 ms (bottom) and 4 ms (top). With longer contact times, new correlation peaks begin to appear, mostly from the quaternary carbons in the 120–160 ppm range.

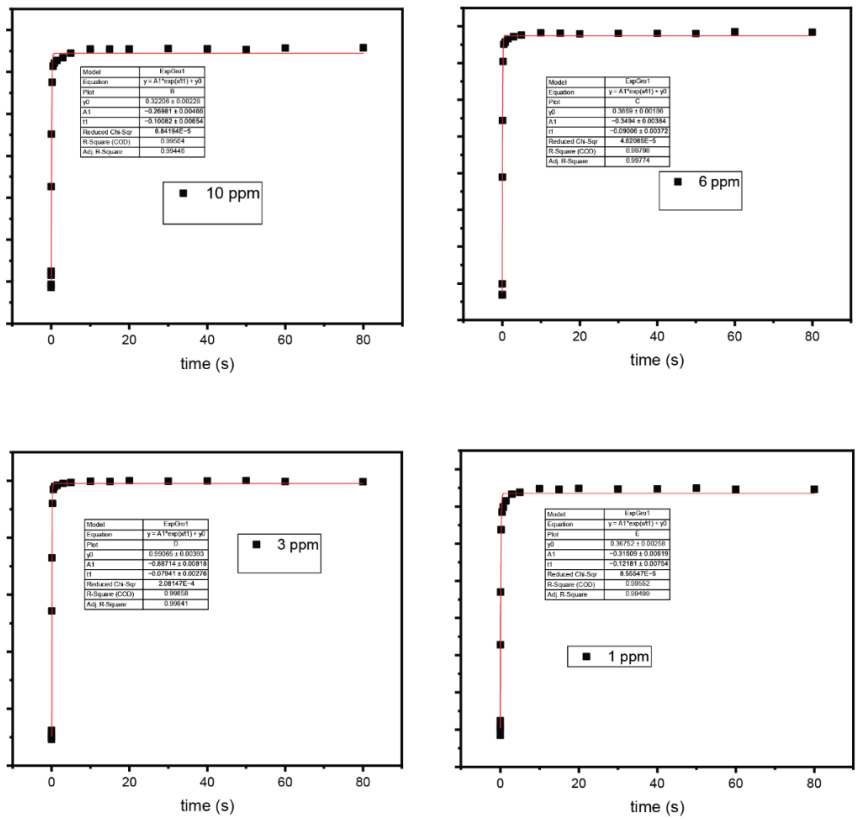

Figure S32: T_1 measurement of the DHICA-melanin at collected at 60 kHz spinning speed.

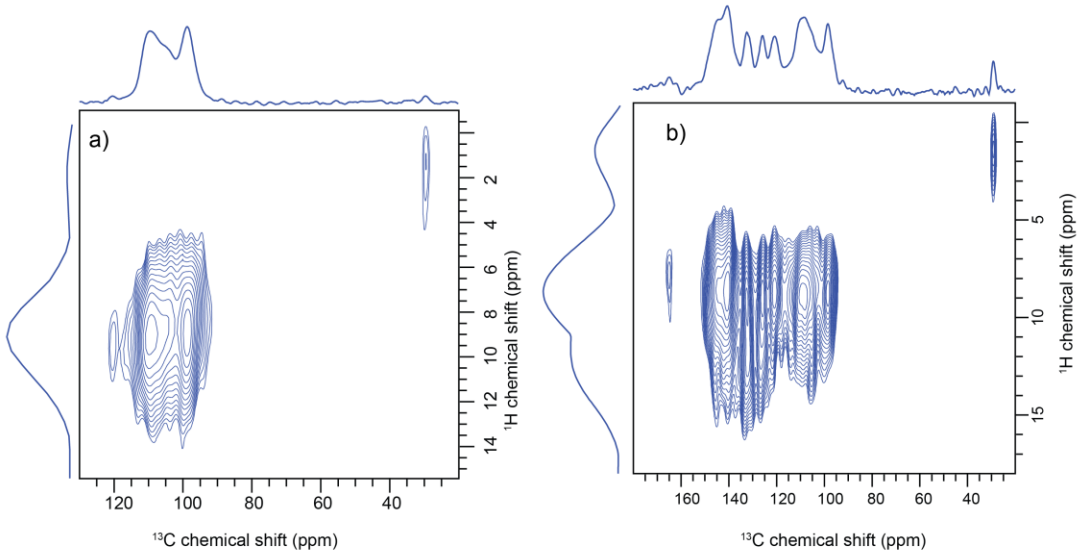

Figure S33: The ^{1}H-^{13}C HETCOR spectra of the unlabelled DHICA-melanin collected at a contact time of a) 0.1 ms b) 2 ms at 24 kHz spinning speed. At long contact time new correlation with quaternary carbons and carbonyl group is observed. Aliphatic peaks are observed in the ^{1}H-^{13}C HETCOR spectra, which could be from the unlabelled carbons in the polymer suggesting the presence of saturated indoline(s).

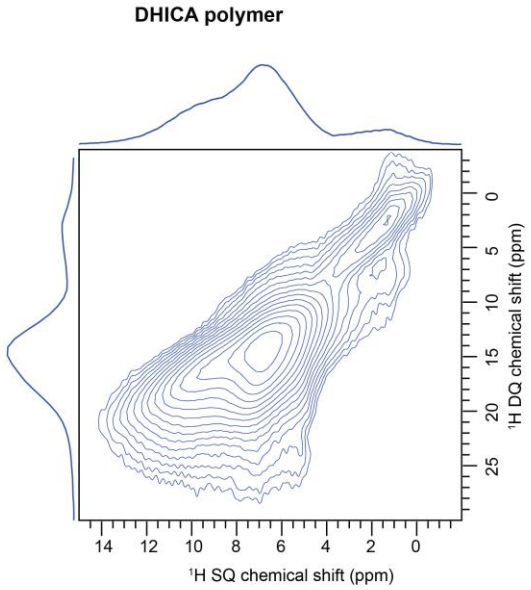

Figure S34: The 2D ^{1}H dipolar double-quantum – single-quantum (DQ-SQ) spectrum of DHICA-melanin collected at 60 kHz spinning speed. A correlation is observed between the aliphatic peak and the aromatic peak indicating the spatial proximity.

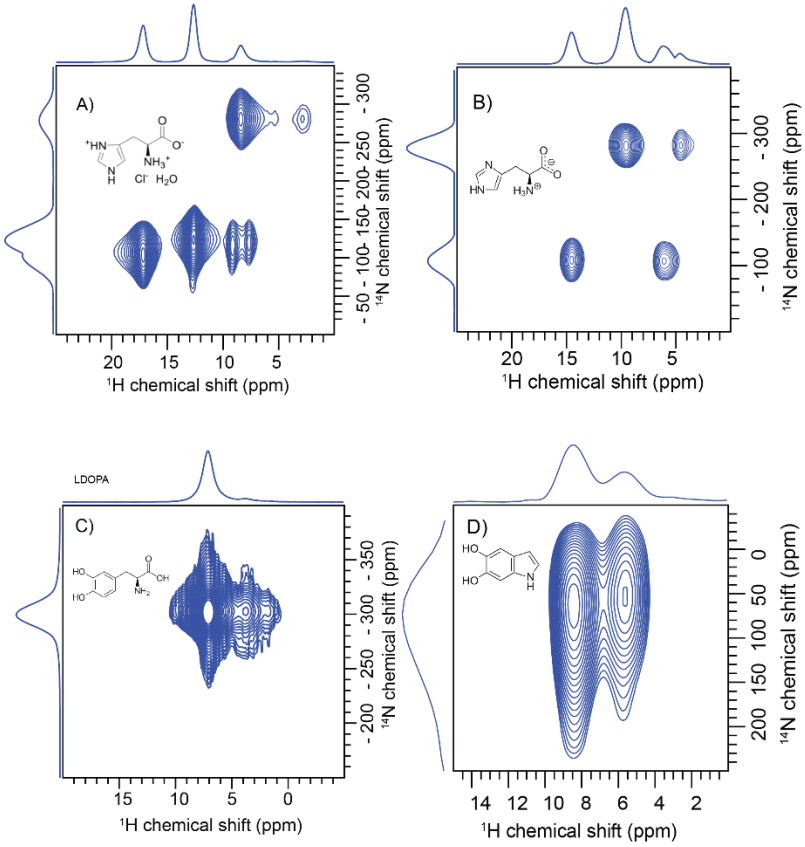

Figure S35: The ^{1}H{^{14}N} DHMQC spectra of A) Histidine-C) L-DOPA[1] and) DHI. The quadrupolar coupling constant Cq for the histidine and L-DOPA is around 1 MHz.

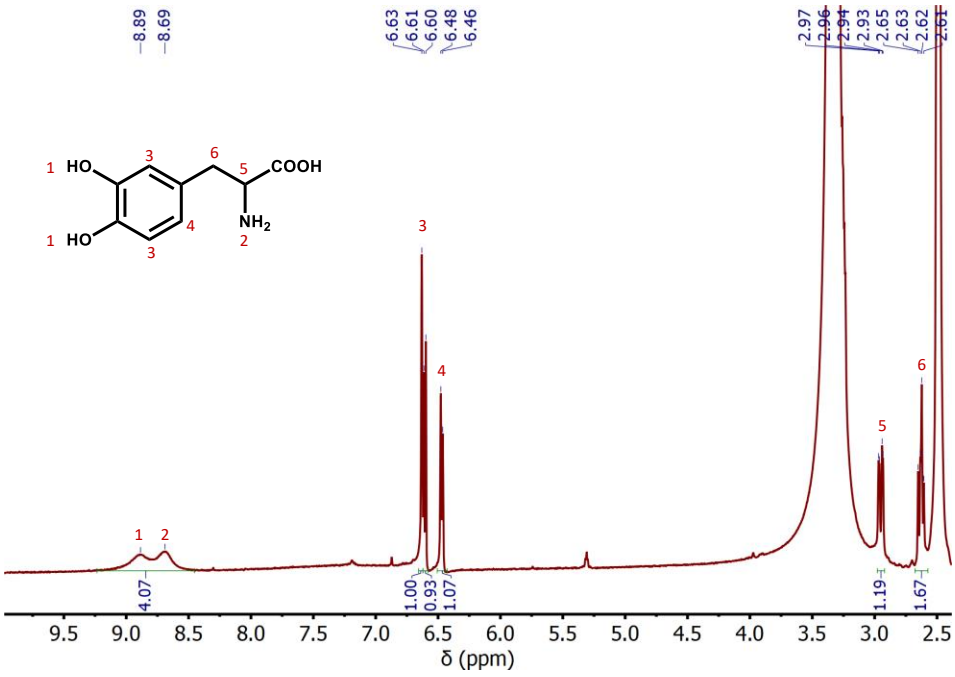

Figure S36: The ^{1}H-NMR spectra of L-DOPA in DMSO-d6 solvent.

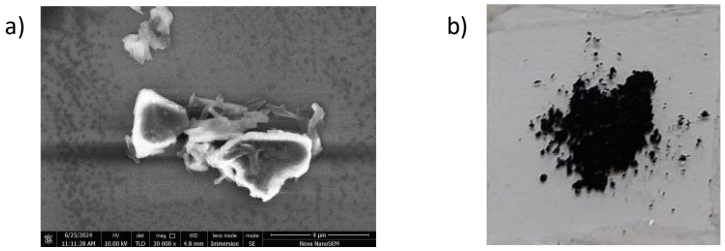

Figure S37: a) The SEM image and b) optical image of DHICA-melanin.

References

1 ELDIX Software Suite Version 0.14.0, ELDICO Scientific AG, **2022**.
2 Apex Suite of Crystallographic Software APEX4, Version 2022, Bruker AXS Inc, **2022**.
3 SADABS, Version 2016/2, Bruker AXS Inc., **2016**.
4 SAINT Version 8.40 B, Bruker AXS Inc, **2019**.
5 G. M. Sheldrick, *Acta Crystallogr. Sect. A* **2015**, *71*, 3–8.
6 C. B. Hübschle, G. M. Sheldrick, B. Dittrich, *J. Appl. Crystallogr.* **2011**, *44*, 1281–1284.
7 T. Bräuniger, P. Wormald, P. Hodgkinson, *Monatshefte für Chemie* **2002**, *133*, 1549–1554.
8 A. Lesage, M. Bardet, L. Emsley, *J. Am. Chem. Soc.* **1999**, 121, 10987-10993.
9 L.-M. Peng, *Micron* **1999**, *30*, 625–648.
10 G. Metz, X. Wu, S. O. Smith, *J Magn Reson A* **1994**, *110*, 219–227.
11 W. Kolodziejski, J. Klinowski, *Chem Rev* **2002**, *102*, 613–628.
12 B. M. Fung, A. K. Khitrin, K. Ermolaev, *Journal of Magnetic Resonance* **2000**, *142*, 97–101.
13 D. Sakellariou, A. Lesage, P. Hodgkinson, L. Emsley, *Chem Phys Lett* **2000**, *319*, 253–260.
14 C. Fernandez, D. P. Lang, J. P. Amoureux, M. Pruski, *J Am Chem Soc* **1998**, *120*, 2672–2673.
15 P. Raval, J. Trébosc, T. Pawlak, Y. Nishiyama, S. P. Brown, G. N. Manjunatha Reddy, *Solid State Nucl Magn Reson* **2022**, *120*, 101808.